

Novel Deep Convolution Neural Network Applied to MRI Cardiac Segmentation.

Clément Zotti¹, Zhiming Luo¹, Alain Lalande², Olivier Humbert³, and Pierre-Marc Jodoin¹

Department of Computer Science, University of Sherbrooke, Canada¹
Université, de Bourgogne Franche-Comté, Dijon France²

Department of Nuclear Medicine, Centre Antoine Lacassagne , Nice, France³

Abstract. In this paper, we propose a fully automatic MRI cardiac segmentation method based on a novel deep convolutional neural network (CNN). As opposed to most cardiac segmentation methods which focus on the left ventricle (and especially the left cavity), our method segments both the left ventricular cavity, the left ventricular epicardium, and the right ventricular cavity. The novelty of our network lies in its maximum a posteriori loss function, which is specifically designed for the cardiac anatomy. Our loss function incorporates the cross-entropy of the predicted labels, the predicted contours, a cardiac shape prior, and an a priori term. Our model also includes a cardiac center-of-mass regression module which allows for an automatic shape prior registration. Also, since our method processes raw MR images without any manual preprocessing and/or image cropping, our CNN learns both high-level features (useful to distinguish the heart from other organs with a similar shape) and low-level features (useful to get accurate segmentation results). Those features are learned with a multi-resolution conv-deconv "grid" architecture which can be seen as an extension of the U-Net.

We trained and tested our model on the ACDC MICCAI'17 challenge dataset of 150 patients whose diastolic and systolic images were manually outlined by 2 medical experts. Results reveal that our method can segment all three regions of a 3D MRI cardiac volume in 0.4 second with an average Dice index of 0.90, which is significantly better than state-of-the-art deep learning methods.

Keywords: Convolutional neural networks, MRI Cardiac segmentation

1 Introduction

MRI is the gold standard modality for cardiac assessment [2,23]. In particular, the use of kinetic MR images along the short axis orientation of the heart allows accurate evaluation of the function of the left and right ventricles. For these examinations, one has to delineate the left ventricular endocardium (LV), the left ventricular epicardium (or myocardium - MYO) and the right ventricular endocardium (RV) in order to calculate the volume of the cavities in diastole and systole (and thus the ejection fraction), as well as the myocardial mass [8]. These parameters are mandatory to detect and quantify different pathologies.

As of today, the clinical use of cardiovascular MRI is hampered by the amount of data to be processed (often more than 10 short axis slices and more than 20 phases per slice). Since the manual delineation of all 3D images is clinically impracticable, several semi-automatic methods have been proposed, most of which being based on active contours, dynamic programming, graph cut or some atlas fitting strategies [3,4,8,9,18]. Unfortunately, these methods are far from real time due to the manual interaction which they require. Also, most of it are ill-suited for segmenting simultaneously the LV, the RV, and the MYO.

So far, a limited number of fully-automatic cardiac segmentation methods have been proposed. While some use traditional image analysis techniques like the Hough transform [7] or

level sets [14], fully-automatic segmentation methods are usually articulated around a machine learning method [3], and more recently deep learning(DL) and convolutional neural networks (CNN) [22]. Among the best CNN segmentation models are those involving a series of convolutions and pooling layers followed by one[15] or several[17] deconvolution layers. In 2015, Ronneberger et al. [19] proposed the U-Net, a CNN which involves connections between the conv and deconv layers and whose performances on medical images are astonishing. Recently, DL methods have been proposed to segment cardiac images[22,6,16]. While Tran[22] applied the well-known fCNN[15] on MR cardiac images, Tan et al.[6] used CNN to localize (but not segment) the LV, and Ngo et al.[16] use deep belief nets again to localize but not segment the LV.

In this paper we propose the first CNN method specifically designed to segment the LV, RV and MYO without a third party segmentation method. Our approach incorporates a shape prior whose registration on the input image is learned by the model. Following a Bayesian formulation, our loss function involves 4 terms, all specifically designed for the purpose of cardiac segmentation.

2 Our Method

The goal of our method is to segment the LV, the RV and the MYO of a 3D $N \times M \times H$ raw MR image X . This is done by predicting a 3D label map T also of size $N \times M \times H$ and whose voxels $\mathbf{v} = (i, j, k)$ contain a label $T_{\mathbf{v}} \in \{\text{Back}, \text{LV}, \text{RV}, \text{MYO}\}$, where "Back" stands for tissues different than the other three. Here we assume that X has been acquired following the common clinical SSFP cine-MRI sequence with a series of short axis slices starting from the mitral valves down to the apex [11] (c.f. Sec 3.1). In order to enforce a clinically plausible result, our method is provided a shape prior S which encapsulates the relative position of the LV, RV and MYO. The main challenge when using a shape prior such as this one is to correctly align it onto the input data X [21]. Since the size and the orientation of the heart does not vary much from one patient to another, we register S on X by translating the center of S on the cardiac center of mass (CoM) \mathbf{c} of X . The CoM is computed based on the location of the pericardium (obtained from MYO and RV) in each slice. Since \mathbf{c} is not provided with the input image, our method has a regression module designed to predict it.

2.1 Shape prior

The shape prior S is a 3D volume which encodes the probability of a 3D location $\mathbf{v} = (i, j, k)$ of being part of a certain class (Back, LV, RV, or MYO). We estimate this probability by computing the pixel-wise empirical proportion of each class based on the groundtruth label fields T_i of the training dataset:

$$P(\mathcal{C}|\mathbf{v}) = \frac{1}{N_t} \sum_{i=1}^{N_t} \mathbf{1}_{\mathcal{C}}(T_{i,\mathbf{v}})$$

where $\mathbf{1}_{\mathcal{C}}(T_{i,\mathbf{v}})$ is an indicator function which returns 1 when $T_{i,\mathbf{v}} = \mathcal{C}$ and 0 otherwise, and N_t is the total number of training images.

These probabilities are put into a $3 \times 20 \times 100 \times 100$ volume S where 3 stands for the 3 classes (RV, MYO, LV)¹, 20 stands for the number of interpolated slices (from the base to the apex) and 100×100 is the inplane size. Note that prior to compute S , we realign the CoM of all training label fields T_i into a common space and crop a 100×100 region around that center.

¹ No need to store the probability of "Back" since the 4 probabilities sum up to 1.

2.2 Probabilistic Formulation

Our training set contains N 3D images $\mathbf{X} = \{X_1, \dots, X_N\}$ with their associated label fields $\mathbf{T} = \{T_1, \dots, T_N\}$, their cardiac CoM $\mathbf{c} = \{c_1, \dots, c_N\}$, as well as a precomputed shape prior S . In order to improve the segmentation accuracy near the border of the LV, RV and MYO, the training set also includes the contour map of each region $\mathbf{C} = \{C_1, \dots, C_N\}$ where $C_{n,\mathbf{v}} = T_{n,\mathbf{v}}$ for every voxel \mathbf{v} located on the border of the LV, RV, or MYO, and $C_{n,\mathbf{v}} = 0$ otherwise.

We train the parameters \mathbf{w} of our CNN with a maximum a posteriori

$$\mathbf{w} = \arg \max_{\mathbf{w}} P(\mathbf{w}|\mathbf{X}, \mathbf{T}, \mathbf{c}, \mathbf{C}, S) \quad (1)$$

which we can reformulate as follows according to the Bayes theorem

$$\mathbf{w} = \arg \max_{\mathbf{w}} \frac{P(\mathbf{X}, \mathbf{T}, \mathbf{c}, \mathbf{C}, S|\mathbf{w})P(\mathbf{w})}{P(\mathbf{X}, \mathbf{T}, \mathbf{c}, \mathbf{C}, S)}. \quad (2)$$

Since $P(\mathbf{X}, \mathbf{T}, \mathbf{c}, \mathbf{C}, S)$ is independent of \mathbf{w} and following the principles of the joint and conditional probabilities, we can reformulate the optimization criterion:

$$\mathbf{w} = \arg \max_{\mathbf{w}} P(\mathbf{C}|\mathbf{X}, \mathbf{c}, \mathbf{T}, S, \mathbf{w})P(\mathbf{T}|\mathbf{X}, \mathbf{c}, S, \mathbf{w})P(\mathbf{c}|\mathbf{X}, S, \mathbf{w})P(\mathbf{X}, S|\mathbf{w})P(\mathbf{w}).$$

Since \mathbf{X} and S are fixed, we can assume that $P(\mathbf{X}, S|\mathbf{w})$ is a constant and remove it from the equation. Also, since the CoM \mathbf{c} depends only on the parameters \mathbf{w} and the content of the image X , we get that $P(\mathbf{c}|\mathbf{X}, S, \mathbf{w}) = P(\mathbf{c}|\mathbf{X}, \mathbf{w})$. Furthermore, since the predicted contour C_i are independent of the center c_i and the shape prior S , we get that

$$\mathbf{w} = \arg \max_{\mathbf{w}} P(\mathbf{C}|\mathbf{X}, \mathbf{T}, \mathbf{w})P(\mathbf{T}|\mathbf{X}, \mathbf{c}, S, \mathbf{w})P(\mathbf{c}|\mathbf{X}, \mathbf{w})P(\mathbf{w}) \quad (3)$$

If we assume that the data from each patient are independent, that $P(c_i|X_i, \mathbf{w})$ follows a Gaussian distribution centered on the true CoM \hat{c}_i and that $P(\mathbf{w})$ is a zero-centered Gaussian, we get that the best \mathbf{w} shall minimize this loss:

$$\mathcal{L} = \sum_i \underbrace{-\ln P(C_i|X_i, T_i, \mathbf{w})}_{\mathcal{L}_C} - \underbrace{\ln P(T_i|X_i, c_i, S, \mathbf{w})}_{\mathcal{L}_T} + \underbrace{\gamma_c \|c_{i,\mathbf{w}} - \hat{c}_i\|^2}_{\mathcal{L}_c} + \underbrace{\gamma_w \|\mathbf{w}\|^2}_{\mathcal{L}_w} \quad (4)$$

where \mathcal{L}_T and \mathcal{L}_C are the log-likelihood of the predicted labels and predicted contours, \mathcal{L}_c is the Euclidean distance between the predicted CoM $c_{i,\mathbf{w}}$ and the true CoM, and \mathcal{L}_w is the prior loss. \mathcal{L}_T implements the following cross-entropy

$$\mathcal{L}_T = -\ln P(T_i|X_i, c, S, \mathbf{w}) = -\gamma_T \sum_{l=1}^4 \sum_{\mathbf{v}} T_{i,l,\mathbf{v}} \ln \hat{T}_{l,\mathbf{v}}$$

where l is the class index, \mathbf{v} is a pixel location, γ_T is a constant, $T_{i,l,\mathbf{v}}$ is the true probability that pixel \mathbf{v} is in class l , and $\hat{T}_{i,l,\mathbf{v}}$ is the output of our model for pixel \mathbf{v} and class l . The contour loss is also a cross-entropy

$$\mathcal{L}_C = -\ln P(C_i|X_i, T_i, \mathbf{w}) = -\gamma_C \sum_{l=1}^4 \sum_{\mathbf{v}} C_{i,l,\mathbf{v}} \ln \hat{C}_{i,l,\mathbf{v}}$$

where C_i and \hat{C}_i are contours extracted from T_i and \hat{T}_i , and γ_C is a constant.

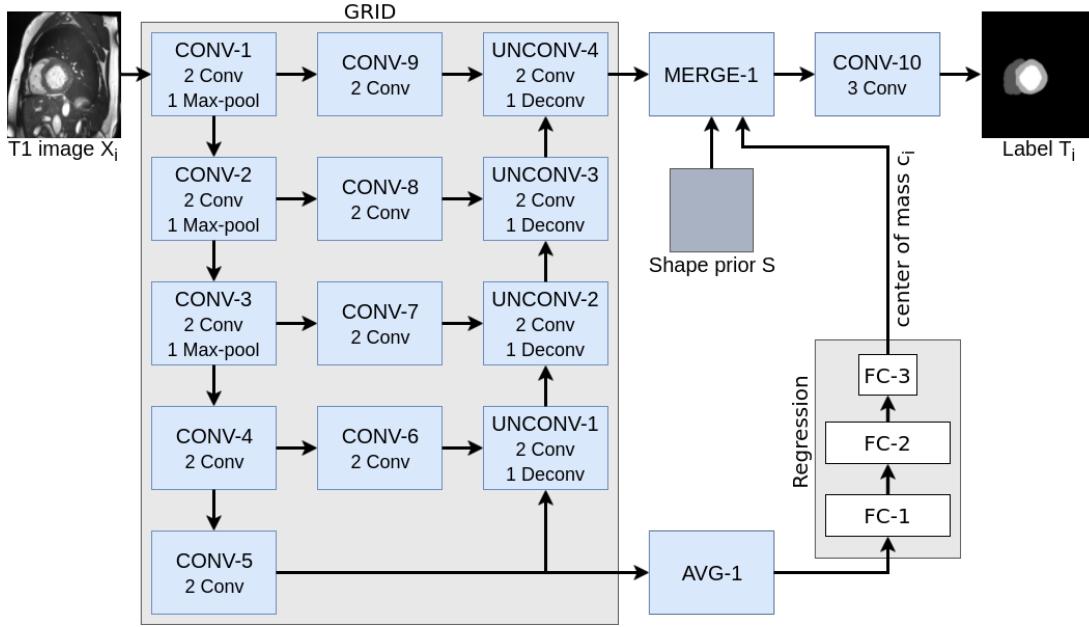


Fig. 1: Our network architecture.

2.3 Proposed network

The goal of our CNN is to minimize the loss \mathcal{L} . To do so, the network has to learn good features for predicting the label field T_i as well as the CoM c_i which is used to align the shape prior S on the input image X_i . Good features must account for both the global and the local context: the global context to differentiate the heart from the surrounding organs and estimate its CoM, and the local context to ensure accurate segmentation. In that perspective, we implemented a grid-like CNN network with 3 columns and 5 rows (c.f. Fig. 1). The input to our model (upper left) is an 256×256 MR image X_i while the output is the CoM c_i (bottom right) and a label field T_i (top right) also of size 256×256 . Note that a common issue with MRI cardiac images is the fact that along the 2D short-axis, the location of the heart sometimes get shifted from one slice to another due to different breath-holds during successive acquisitions (c.f. supplementary material for an example). As a consequence, instead of processing a 3D volume as a whole, we feed the network with 2D slices as shown in Fig. 1 and reshape the 3D volume T_i by stacking up the resulting 2D label fields.

As we get deeper in the network (from CONV-1 to CONV-5), the extracted features involve a larger context of the input image. Since the CONV-5 layer includes high-level features from the entire image, we use it to predict the cardiac CoM c_i of the input image X_i . The second column contains 4 convolution layers (all without max-pooling) used to compute features at various resolutions. The last column aggregates features from the lowest to the highest resolution. The UNCONV-4 layer contains both global and local features which we use to segment the image. Note that this grid structure is similar to the U-Net except for the middle CONV-6 to 9 layers and the fact that we use the CONV-5 features to estimate a CoM c_i . Each conv layer has a 3×3 receptive field and its feature maps have the same size than their input (zero padding).

We also batch normalize each feature map, use the ReLU activation function, and dropout[20] to prevent overfitting.

Estimating the center of mass c_i The CoM c_i is estimated with a regression module located after the CONV-5 layer. An average pooling layer (AVG-1) is used to reduce the number of features fed to the FC-1 layer. The FC-1, FC-2 and FC-3 layers are all fully connected and the output of FC-3 is the (x_i, y_i) prediction of c_i .

Estimating the label field T_i The output of the UNCONV-4 layer has 4 256×256 feature maps which we append to the shape prior S . The MERGE-1 layer realigns S based on the estimated CoM c_i and use zero padding to make sure S has a 256×256 inplane size. In this way, the output of MERGE-1 has 7 feature maps: 4 from UNCONV-4 and 3 from S . The last CONV-10 layer is used to squash those 7 feature maps down to a 4D output.

Training The model is trained by minimizing the loss \mathcal{L} with a batch size of 10 2D MR images and with the ADAM optimizer [12]. The model is trained with a learning rate of 10^{-4} during 150 epochs.

Pre and Post processing The input 3D images X are pre-processed by clamping the 4% outlying grayscale values, zero-centering the grayscales and normalize it by their standard deviation. Once training is over, each predicted label field T_i is post-processed with the aligned shape prior S . This allows to check where T_i and S overlap and thus remove false predictions. We also apply a convex hull on each slice of T_i to remove concavities.

3 Experimental Setup and Results

3.1 Dataset, evaluation criteria, and other methods

Our system was trained and tested on the ACDC MICCAI'17 dataset², made of 150 exams (all from different patients) acquired from two MRI scanners (1.5T and 3.0T, Siemens Medical Solution, Erlangen, Germany). 100 exams were used for training and 50 for testing. The exams are divided into 5 evenly distributed groups: dilated cardiomyopathy, hypertrophic cardiomyopathy, myocardial infarction with altered left ventricular ejection fraction, abnormal right ventricle and patients without cardiac disease. Cine MR images were acquired in breath-hold with a retrospective or prospective gating and with a SSFP sequence in 2-chambers, 4-chambers and in short axis orientations. A series of short axis slices cover the LV from the base to the apex, with a thickness of 5 to 8mm and sometimes an interslice gap of 5 mm. The spatial resolution goes from 0.83 to 1.75 mm²/pixel. The reconstructed 3D images of the diastolic and the systolic phases come with a pixel-accurate manual delineation by two independent medical experts of each cardiac region. The delineation of these regions follows well-defined rules (such as the inclusion of the papillary muscles) widely accepted in cardiology [13].

In order to gauge performances, we report the usual clinical and geometrical metrics used in cardiology [13]. The clinical metrics are the average ejection fraction (EF) error, the average LV and RV systolic and diastolic volume errors, and the average myocardial mass error. As for the geometrical metrics, we report the Dice [5] and the Hausdorff distances [10] for all 3 regions.

We compared our method with two recent CNN methods: the conv-deconv CNN by Noh et al. [17] and the U-Net by Ronneberger et al. [19]. We chose those methods based on their

² <http://acdc.creatis.insa-lyon.fr>

Table 1: Geometrical and clinical results for the testing dataset.

Area	Dice			Hausdorff (mm)		
	LV	RV	MYO	LV	RV	MYO
ConvDeconv	0.91±0.05	0.79±0.15	0.82±0.06	16.03±22.3	28.53±17.8	25.78±30.5
U-Net	0.93±0.05	0.85±0.14	0.87±0.04	14.96±19.8	21.4±17.1	25.58±32.8
Our method	0.94±0.04	0.88±0.08	0.89±0.03	5.79±3.6	16.78±14.0	10.82±14.6

Area	EF error (%)		LVV error (mL)		RVV error (mL)		Mass error (g)	
	LV	RV	Dia	Sys	Dia	Sys	Dia	Sys
ConvDeconv	3.53±3	9.70±11	7.02±7	7.93±8	27.71±31	25.07±33	16.52±20	18.17±21
U-Net	3.16±3	12.94±29	7.29±8	8.45±10	19.47±37	19.98±29	12.55±13	15.68±15
Our method	2.98±3	9.54±9	5.09±4	5.74±6	10.13±12	18.7±17	11.59±6	8.73±7

excellent segmentation capabilities but also because they are a particular case of our approach (c.f. supplementary material). Our code based on Keras [1] and database will be made available upon acceptance of this paper.

3.2 Experimental results

Our method outperforms both the conv-deconv and the U-Net on every metric (Table 3). While the Dice score of the U-Net is close to our’s, the Hausdorff distance is significantly lower for our method by an average of 9.5 mm. This is a strong indication that the contour loss and the shape prior help improving results, especially close to the boundaries. Without much surprise, the RV is the most challenging organ, mostly because of its complicated shape, the partial volume effects close to the free wall, and intensity inhomogeneities. The clinical metrics are also in favor of our method. Here again, although the EF error of our method is close to the other ones, our method is significantly better on other metrics such as the diastolic RV volume error and the MYO mass error (c.f. supplementary material for per-pathology detailed results).

The fact that our method gets similar (although better) Dices and EF error but much better Hausdorff distances can be explained as follows. While all three methods often produce similar 2D segmentation label fields, the conv-deconv and U-Net frequently produce degenerated 2D label fields. Since those erroneous results affect only 1 or 2 slices out of 10 to 30, it does not affect much the overall estimated volume nor the EF. However, a poorly segmented slice induces a large Hausdorff distances. On average, our method gets a poor segmentation (Hausdorff > 20mm, in general at basal level where the separation between the cavity and the vessel root is not clearly defined) on only 10% of the patients compared with 37% for conv-deconv and 30% for the U-Net. In Fig. 2, the first row shows a slice for which all three methods performed well. The second and third rows show slices for which the conv-deconv and the U-Net produce degenerated results (on the 2nd row the RV is missing and on the 3rd row we get anatomically impossible results).

4 Conclusion

We proposed a new CNN method specifically designed for MRI cardiac segmentation. It implements a ”grid” architecture with is a generalization of the U-net. It also use a shape prior which is automatically aligned on the input image with a regression method. The shape prior forces the method to produce anatomically plausible results. Results show that our method could be used in daily clinical practice for the calculation of important functional parameters

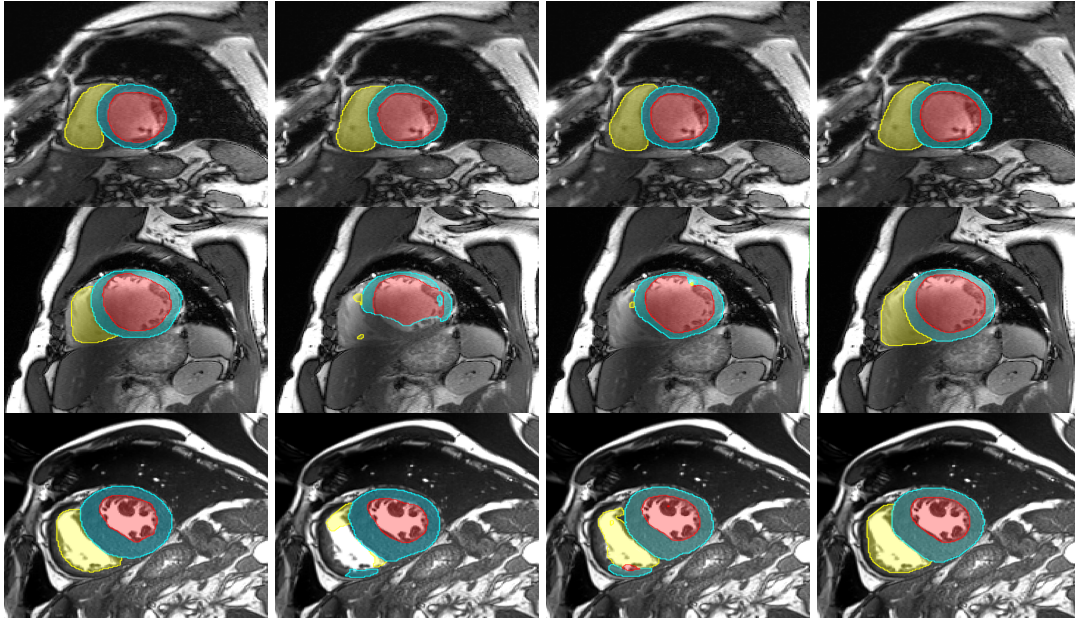


Fig. 2: From left to right: ground truth, conv-deconv, U-Net, and our method.

of the heart. In the future, we plan on generalizing our method to other modalities (such as echocardiography and CT-scan) as well as other organs such as the brain. In that case, we shall propose a more elaborate registration module which shall implement an affine transformation.

References

1. François Chollet et al. Keras. <https://github.com/fchollet/keras>, 2015.
2. F. H. Epstein. Mri of left ventricular function. *J of nuc. card*, 14(5):729–744, 2007.
3. C. Petitjean et al. Right ventricle segmentation from cardiac mri: A collation study. *Med. Image Anal.*, 19(1):187–202, 2015.
4. D. A. Auger et al. Semi-automated left ventricular segmentation based on a guide point model approach for 3d cine dense cardiovascular magnetic resonance. *J. of Card. Mag. Res.*, 16(1):8, 2014.
5. K. H. Zou et al. Statistical validation of image segmentation quality based on a spatial overlap index 1: Scientific reports. *Aca. rad.*, 11(2):178–189, 2004.
6. L. K. Tan et al. Cardiac left ventricle segmentation using convolutional neural network regression. In *Proc. of IECBES*, pages 490–493. IEEE, 2016.
7. L. Wang et al. Left ventricle: Fully automated segmentation based on spatiotemporal continuity and myocardium information in cine cardiac magnetic resonance imaging (lv-fast). *BioMed Res. Int.*, 2015, 2015.
8. P. Peng et al. A review of heart chamber segmentation for structural and functional analysis using cardiac magnetic resonance imaging. *MAGMA*, 29(2):155–195, 2016.
9. D. Grosgeorge, C. Petitjean, J.-N. Dacher, and S. Ruan. Graph cut segmentation with a statistical shape model in cardiac mri. *CVIU*, 117(9):1027–1035, 2013.
10. D.P. Huttenlocher, G.A. Klanderman, and Rucklidge W.J. Comparing images using the hausdorff distance. *IEEE(PAMI)*, 15(9):850–863, 1993.

11. B. Kastler. Cardiovascular anatomy and atlas of mr normal anatomy. In *MRI of Cardiovascular Malformations*, chapter 2, pages 17–39. Springer, 2011.
12. D. Kingma and J. Ba. Adam: A method for stochastic optimization. In *Proc. of ICLR*, 2015.
13. A. Lalande, M. Garreau, and F. Frouin. Evaluation of cardiac structure segmentation in cine magnetic resonance imaging. In *Multi-Modality Cardiac Imaging*, pages 169–215. ISTE-Wiley, 2015.
14. Y. Liu and G. Captur et al. Distance regularized two level sets for segmentation of left and right ventricles from cine-mri. *Mag. res. img.*, 34(5):699–706, 2016.
15. J. Long, E. Shelhamer, and T. Darrell. Fully convolutional networks for semantic segmentation. In *Proc. of CVPR*, pages 3431–3440, 2015.
16. T. A. Ngo, Z. Lu, and G. Carneiro. Combining deep learning and level set for the automated segmentation of the left ventricle of the heart from cardiac cine magnetic resonance. *Med. Image Anal.*, 35(1):159–171, 2017.
17. H. Noh, S. Hong, and B. Han. Learning deconvolution network for semantic segmentation. In *Proc. of ICCV*, 2015.
18. C. Petitjean and J.N. Dacher. A review of segmentation methods in short axis cardiac mr images. *Med. Image Anal.*, 15(2):169–184, 2011.
19. O. Ronneberger, P. Fischer, and T. Brox. U-net: Convolutional networks for biomedical image segmentation. In *in Proc. of MICCAI*, pages 234–241, 2015.
20. N. Srivastava and G. Hinton et al. Dropout: a simple way to prevent neural networks from overfitting. *J. of Mach. Learn. Res.*, 15:1929–1958, 2014.
21. V. Tavakoli and A. A. Amini. A survey of shaped-based registration and segmentation techniques for cardiac images. *CVIU*, 117(9):966–989, 2013.
22. P. V. Tran. A fully convolutional neural network for cardiac segmentation in short-axis mri. *arXiv preprint arXiv:1604.00494*, 2016.
23. G. W. Vick. The gold standard for noninvasive imaging in coronary heart disease: magnetic resonance imaging. *Cur. op. in card.*, 24(6):567–579, 2009.

Supplementary material

Ejection Fraction (EF) The EF is a well known metric for assessing cardiac health. It is computed as follow

$$EF = \frac{V_{dia} - V_{sys}}{V_{dia}}$$

where V_{dia} and V_{sys} are respectively the diastolic and systolic volumes in ml . The EF can be applied both on the LV and on the RV.

Details of our architecture Table 1 shows a detailed description of the layers used in our network.

Table 2: Details of the proposed architecture.

Block	Layer	Kernel	Stride	Output	Block	Layer	Kernel	Stride	Output
CONV-1	2 conv +	3x3	1	256x256x32	UNCONV-1	deconv+			32x32x768
	max-pool	2x2	1	128x128x32		2 conv	2x2	1	32x32x256
CONV-2	2 conv +	3x3	1	128x128x64	UNCONV-2	deconv+			64x64x384
	max-pool	2x2	1	64x64x64		2 conv	2x2	1	64x64x128
CONV-3	2 conv +	3x3	1	64x64x128	UNCONV-3	deconv+			128x128x192
	max-pool	2x2	1	32x32x128		2 conv	2x2	1	128x128x64
CONV-4	2 conv +	3x3	1	32x32x256	UNCONV-4	deconv+			256x256x96
	max-pool	2x2	1	16x16x256		conv+	2x2	1	256x256x32
CONV-5	2 conv	3x3	1	16x16x512		conv	2x2	1	256x256x4
CONV-6	2 conv	3x3	1	32x32x64	AVG-1	Average-pool			512
CONV-7	2 conv	3x3	1	64x64x64	FC-1	Dense	256		256
CONV-8	2 conv	3x3	1	128x128x64	FC-2	Dense	256		256
CONV-9	2 conv	3x3	1	256x256x64	FC-3	Dense	2		2
					MERGE-1	merge prior			256x256x7
					CONV-10	2 conv	3x3		256x256x32
						1 conv	3x3		256x256x4

Other networks' architecture Figure 3a and 3b show a schematic overview of the conv-deconv and U-Net architectures. As can be seen, these two models are a special case of our proposed configuration (c.f. figure 1 in the paper).

Shape prior Figure 4 shows the shape prior S in RGB format. Here red stands for $P(C = RV|\mathbf{v})$, green for $P(C = MYO|\mathbf{v})$, and blue for $P(C = LV|\mathbf{v})$. Note that the long axis view has been vertically stretched for visualization purposes.

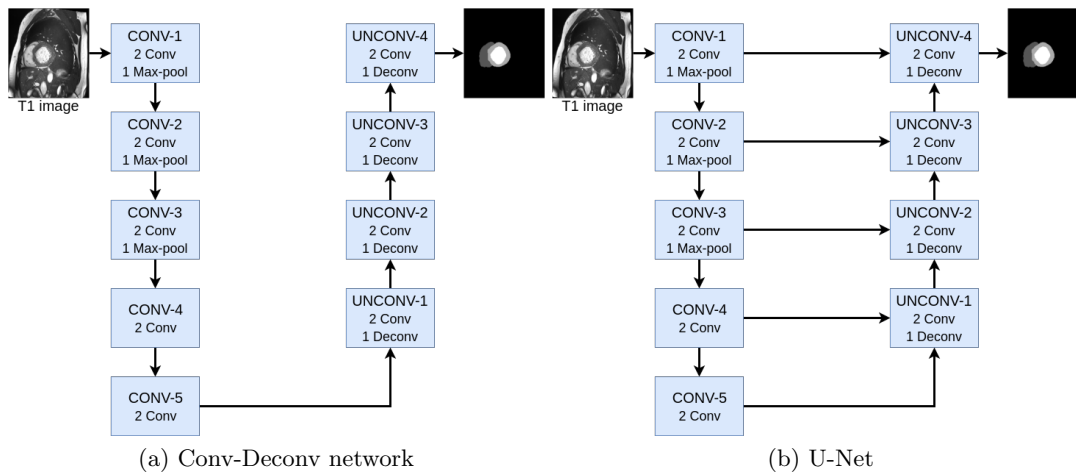


Fig. 3: Schematic representation of the architecture of the Conv-Deconv and the U-Net CNN.

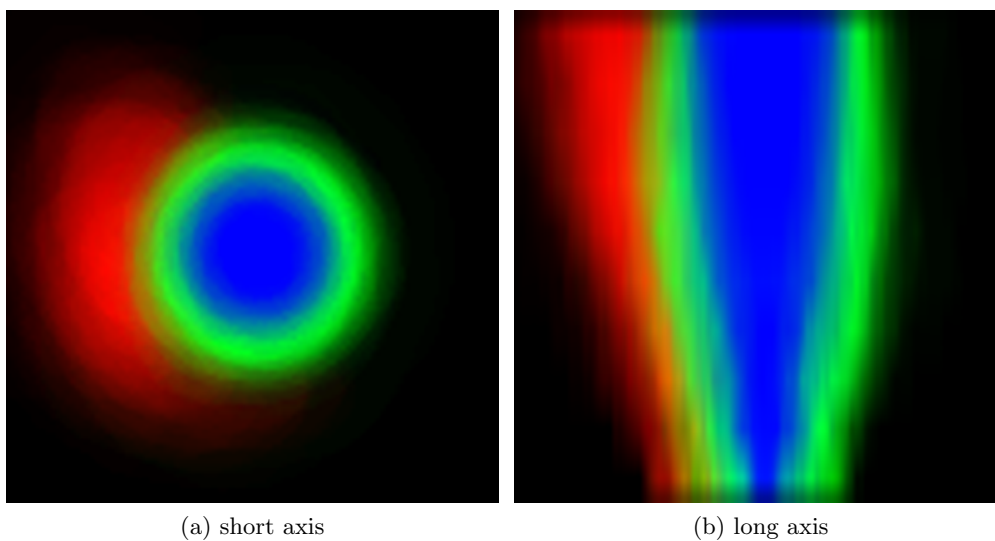


Fig. 4: Illustration of our shape prior probability map.

Connection between a Gaussian and an L2 loss Lets consider a parameter vector \mathbf{w} following a Gaussian likelihood

$$P(\mathbf{w}) = \mathcal{N}(\mathbf{w}; \boldsymbol{\mu}, \Sigma).$$

One can derive the negative log-likelihood as follows

$$\begin{aligned} -\ln P(\mathbf{w}) &= -\ln \mathcal{N}(\mathbf{w}; \boldsymbol{\mu}, \Sigma) \\ &= -\ln \frac{1}{\sqrt{2\pi|\Sigma|}} \exp^{-\frac{1}{2}(\mathbf{w}-\boldsymbol{\mu})^T \Sigma^{-1}(\mathbf{w}-\boldsymbol{\mu})} \\ &= \ln(\sqrt{2\pi|\Sigma|}) - \frac{1}{2}(\mathbf{w}-\boldsymbol{\mu})^T \Sigma^{-1}(\mathbf{w}-\boldsymbol{\mu}) \end{aligned}$$

and if we assume that this distribution is zero-centered, then $\boldsymbol{\mu} = 0$. Also, since $\ln(\sqrt{2\pi|\Sigma|})$ and $\frac{1}{2}\Sigma^{-1}$ are independant of \mathbf{w} , we can replace it by a constant term

$$= cst_1 - cst_2 \|\mathbf{w}\|^2,$$

and by putting this equation in the argmax formulation of Eq.(3) in the paper, we get

$$\mathcal{L}_w = \gamma_w \|\mathbf{w}\|^2$$

where γ_w is a constant.

Misalign images As mentioned in section 2.3, it frequently happens that the patient cannot breath-hold long enough during an MRI acquisition. This creates a shift in the 3D volume which is illustrated in Fig. 5

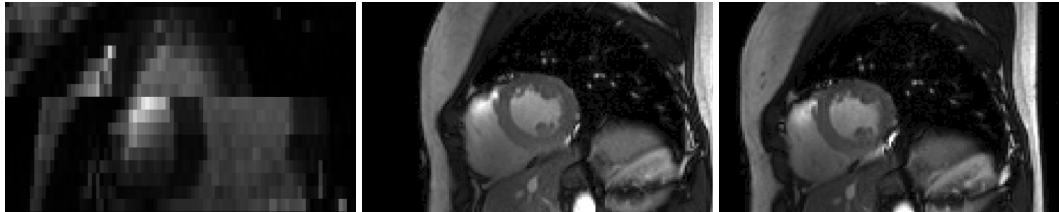


Fig. 5: Example of an image shifted due to a movement or different breath-old during acquisition. This causes a lateral artifact in the 3D volume.

Detailed results Table 3 and 4 contain detailed results for each group of patients, namely dilated cardiomyopathy (DCM), hypertrophic cardiomyopathy (HCM), myocardial infarction with altered left ventricular ejection fraction (MINF), abnormal right ventricle (RV) and patients without cardiac disease (NOR). As far as the geometrical metrics go, our method outperforms the U-Net and the Conv-Deconv methods on every group of patients. It is especially true for the RV group. As for the clinical metrics, our method is globally better than the U-Net and the Conv-Deconv (especially for DCM and RV) but sometime gets slightly worse results, especially for NOR. As mentioned in the paper, the errors produced by the U-Net and the

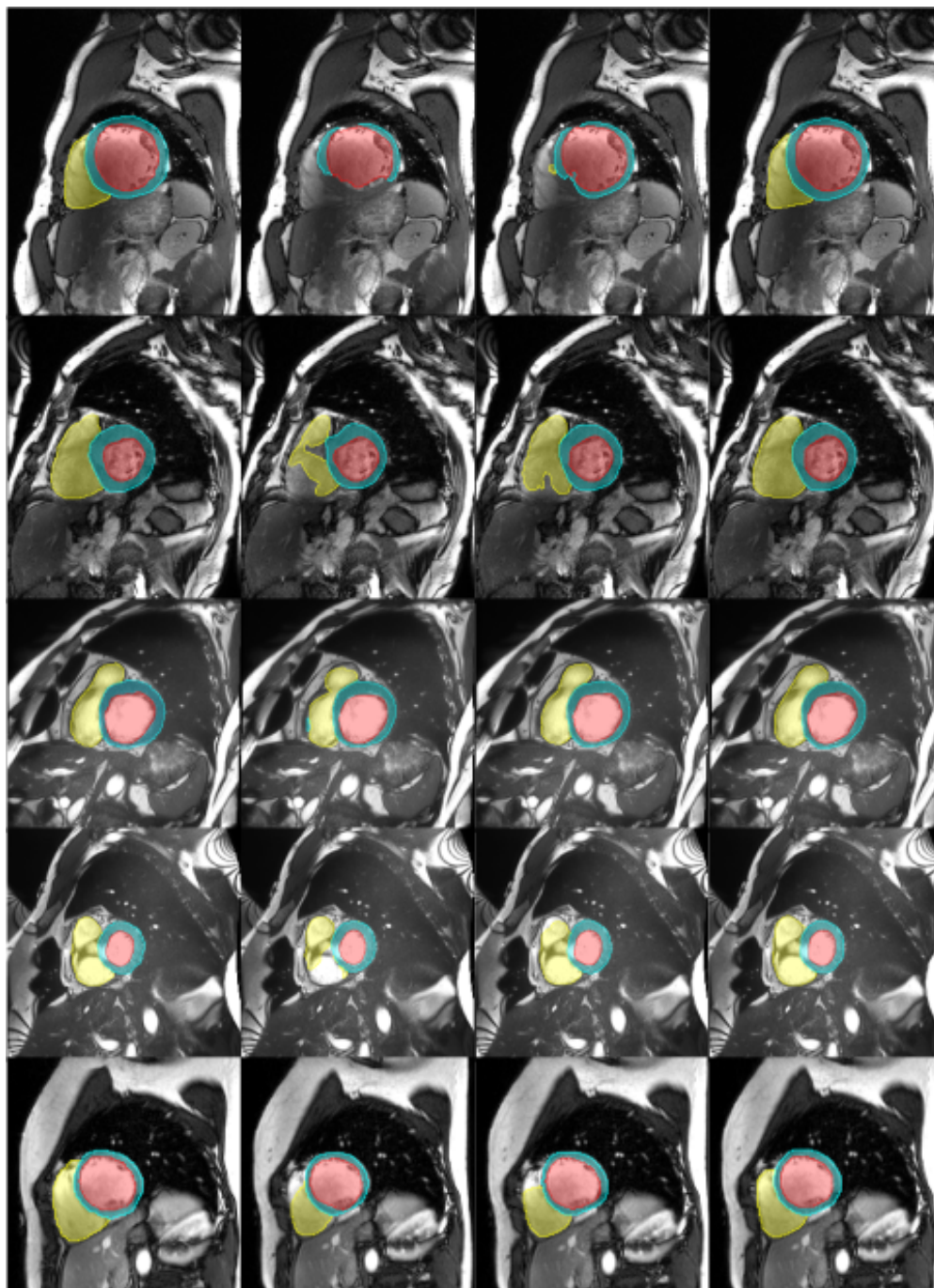


Fig. 6: From top to bottom, DCM, HCM, MINF, NOR, RV and from left to right, ground truth, convdeconv, U-Net, and our method.

Table 3: Geometrical metrics per pathology

		Dice			Hausdorff (mm)		
		LV	RV	MYO	LV	RV	MYO
DCM	Model						
	ConvDeconv	0.95	0.71	0.79	16.53	47.84	23.15
	U-Net	0.95	0.76	0.85	25.02	35.55	25.46
	Our method	0.96	0.89	0.87	7.81	24.37	22.62
HCM	ConvDeconv	0.87	0.77	0.87	14.39	28.27	17.89
	U-Net	0.90	0.85	0.89	14.2	17.17	25.47
	Our method	0.91	0.85	0.90	6.47	16.25	8.39
MINF	ConvDeconv	0.94	0.83	0.81	11.19	22.44	35.98
	U-Net	0.95	0.87	0.85	10.74	17.11	21.92
	Our method	0.96	0.89	0.88	5.01	13.03	6.15
RV	ConvDeconv	0.9	0.8	0.8	20.27	27.0	30.93
	U-Net	0.9	0.87	0.84	27.07	28.22	34.06
	Our method	0.94	0.89	0.87	5.71	17.87	16.55
NOR	ConvDeconv	0.91	0.84	0.83	20.19	18.8	24.2
	U-Net	0.95	0.88	0.87	4.65	14.25	25.78
	Our method	0.94	0.89	0.89	4.08	13.93	5.04

Conv-Deconv networks are often concentrated within 1 or 2 slices in the whole 3D MRI volume. While this might not affect much the EF (especially when a method produces the same erroneous result on the systolic and diastolic volume) and the estimated volume, it has a large impact on the Dice and the Hausdorff metrics.

Results for all three methods obtained on every group of patients are illustrated in Figure 6.

Segmentation error Our method is not void of limitations. While it is most of the time very accurate, it sometimes fails and when it does, it does so at the end points of the heart. As shown on the first row of Figure 7, our method sometimes misses the tip of the apex (here the end of the RV). Another place where our method sometimes fail is close to the valves as shown on the second row of Figure 7. The problem here is that the LV is merged with the aorta leading to a situation extremely hard to delineate, even for a medical expert.

Table 4: Clinical metrics per group. The EF error is in %, the LV and RV volume error are in ml, and the MYO mass errors are in g.

		EF error		LV volume err		RV volume err		MYO mass err	
Model		LV	RV	Dia	Sys	Dia	Sys	Dia	Sys
DCM	ConvDeconv	1.58	14.29	9.81	11.21	53.08	44.86	35.38	34.32
	U-Net	3.18	31.16	9.26	14.51	45.95	35.29	22.89	23.62
	Our method	1.51	7.86	8.46	6.43	7.27	16.3	10.79	9.82
HCM	ConvDeconv	4.38	6.54	5.76	6.51	21.31	15.3	14.92	17.14
	U-Net	2.24	7.24	7.55	4.9	12.34	9.48	12.73	20.77
	Our	3.05	11.04	8.12	6.39	9.87	15.42	10.39	7.89
MINF	ConvDeconv	2.33	7.28	8.81	8.99	16.91	16.2	10.55	9.77
	U-Net	1.88	8.59	8.43	9.82	9.1	12.86	8.86	8.77
	Our method	3.01	10.43	4.48	5.0	7.29	18.45	10.18	7.82
RV	ConvDeconv	6.93	8.32	8.75	9.08	36.76	29.75	8.84	12.5
	U-Net	8.47	5.3	10.96	12.65	25.86	25.29	8.15	11.01
	Our	5.15	9.11	4.75	6.71	19.9	26.38	16.59	6.45
NOR	ConvDeconv	3.79	12.36	3.35	5.01	19.01	25.28	8.08	12.53
	U-Net	2.79	11.61	2.29	3.69	11.57	22.86	6.48	8.91
	Our method	3.06	8.66	3.18	4.68	10.87	20.9	10.06	8.92

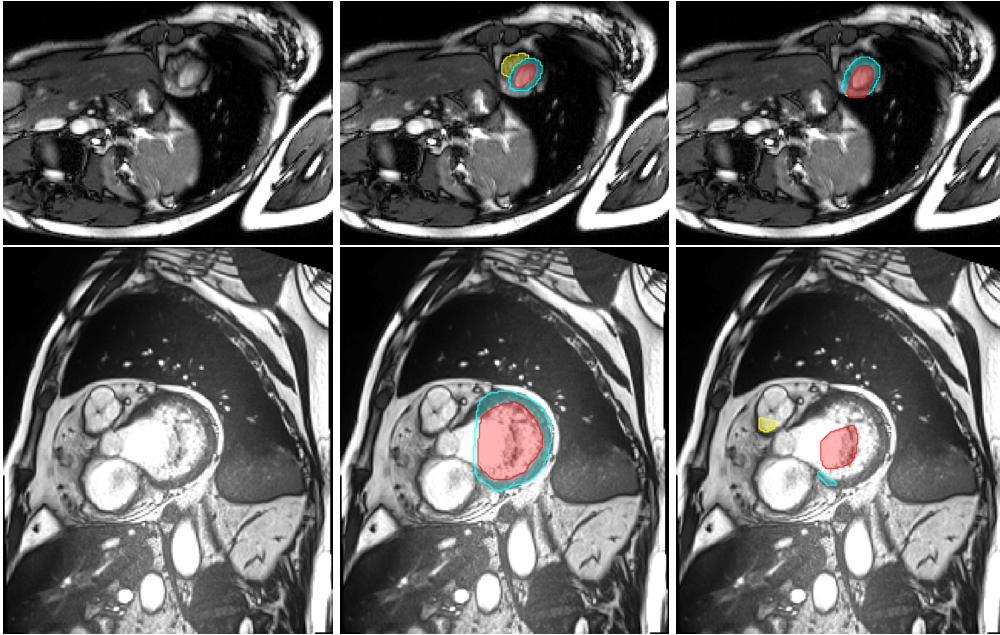


Fig. 7: Erroneous segmentation at the apex and close to the valves. From left to right: raw MR image, ground truth, result from our method.